Activity report of the Italian CRG beamline at the European Synchrotron Radiation Facility (ESRF)

N. 5 - April 2018

Grenoble, April 2018

Responsabile editoriale: Francesco d'Acapito
(*dacapito@iom.cnr.it*)

Editing: Roberta De Donatis
(*roberta.dedonatis@cnr.it*)

ISSN 2553-9248

LISA

Annual Report 2017

Istituto Officina dei Materiali

Abstract

This document resumes the activity of the Italian CRG beamline at ESRF (LISA project) during year 2017. The features of the newly installed instrumentation are presented as well as statistic data on the beamline, highlight experiments and publications.

Keywords

Italian beamline at ESRF, BM08

LISA project

X-ray Absorption Spectroscopy

Index

Foreword

2017 has been a crucial year for LISA. The beamline construction has been carried out in two phases: the first in the period Jan-Mar 2017 concerning the installation of the monochromator and its cryocirculator. Successively, in the second half of the year (and in the first quarter of 2018), the new mirrors have been installed and the new experimental hutch EH2 has been put into operation. All these operations have been carried out by the local staff greatly supported by the IOM technicians (A. Laloni, A. de Luisa, A. Martin) and ESRF technicians (E. Dettona). In the time between these phases, users have carried out experiments with the new monochromator. At present, the beamline is fully operative in the final configuration.

In the activity period of 2017 LISA has carried out 15 experiments for a total 210 shifts. 26 papers have been published from studies carried out at LISA and one Erasmus Placement student (Michela la Bella from Florence University) was hosted during 4 months.

Beamline optics

The beamline optics has been designed to collect (at most) a horizontal fan of 1mrad and a vertical fan of 0.09 mrad, and it is fully compatible with the single Bend source of the future EBS ring. The optical elements are (see Fig.[1]): a cylindrical collimating mirror (M1), a double crystal monochromator (DCM) and a toroidal focusing mirror (M2). Mirrors operate at an incidence angle of 2 mrads and have a Si and a Pt coating to cover a wide range of energies: 5-15 keV for the Si coating and 15-40 keV for the Pt coating. The DCM contains two crystal pairs: Si(311) for experiments needing high energy resolution and Si(111) for experiments needing a high photon flux. M2 focalizes in a 2:1 geometry in order to minimize the aberration effects.

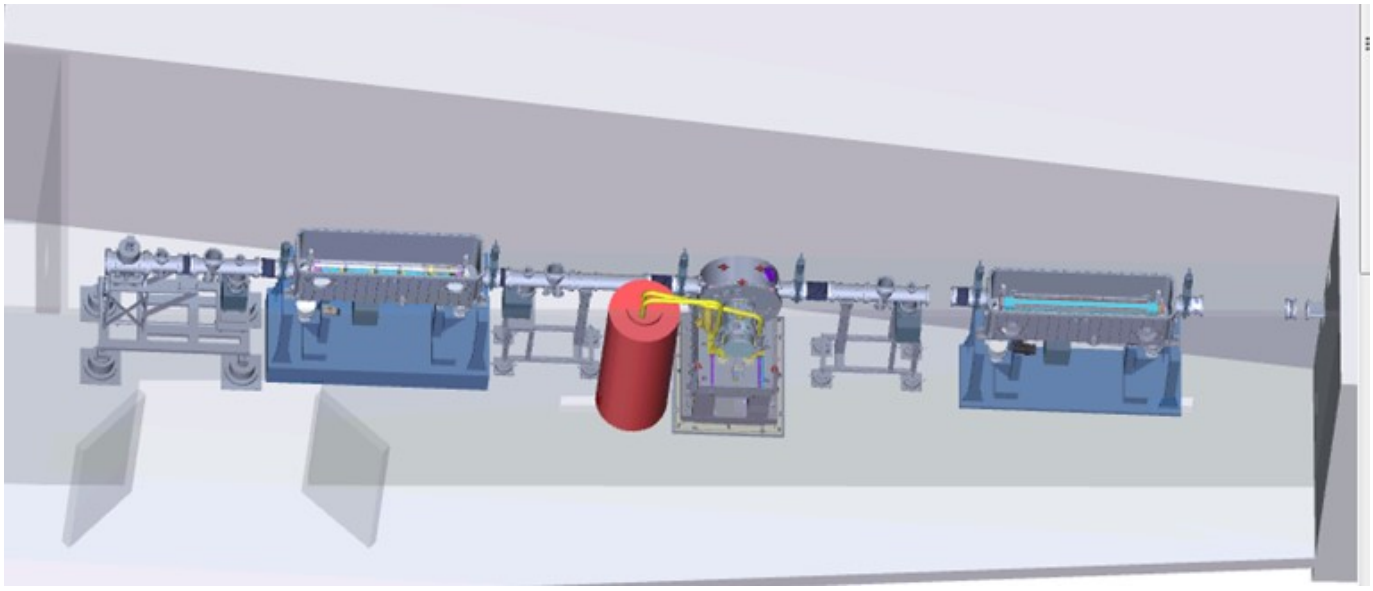

Fig.[1]. Inner view of the optic hutch. From right to left there is M1, the monochromator and M2. The red cylinder is the cryocirculator.

In the following, some preliminary results from the commissioning phase will be presented.

First mirror, M1

M1 has an optical length of 1.3 m and it acts as a collimator. Its radius of curvature has been optimized at the maximum vertical acceptance (2 mm wide slits at 23 m, i.e. about 0.09 mrads) by maximizing monochromator energy resolution looking at the height of a white line of a specific compound (see Fig.[2]).

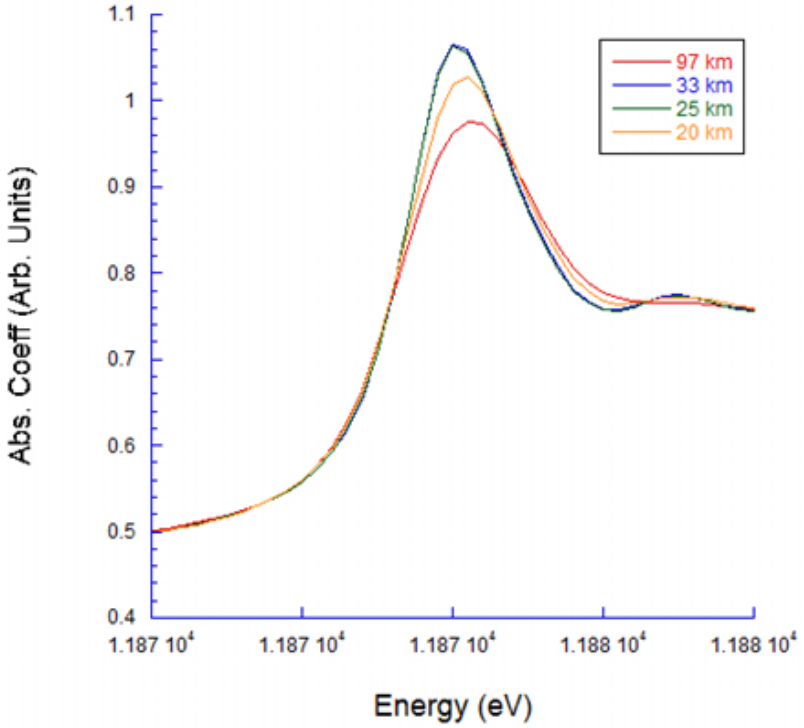

Fig.[2]. Optimization of the radius of curvature of M1 by optimizing the energy resolution of the monochromator. In this case the height of the white line in the As-K edge of a sample of mineral Adamite ($Zn_2(AsO_4)(OH)$) was used. Si(111) crystals were used. The legend indicates the radii of curvature for each spectrum shown in this plot.

The optimal value for the bending radius was easily found by comparison of spectra taken at different radii and, using the calibration of the motor steps vs radius of curvature provided by the manufacturer, it resulted to be 29±4 km, in good agreement with the theoretical value of 25 km.

Monochromator

The monochromator is of the “double crystal fixed exit” type, and it provides access to a wide energy range (4-90 keV) simply by changing the crystals via a horizontal shift. The liquid nitrogen cooling permits to minimize thermal effects due to the changing current in the ring. The thermal contact is realized via copper plates tightened to the crystals with In foils ensuring the thermal contact. The plates of the first crystals are directly cooled, those of the second crystals are cooled via copper brides. The crystals mechanical mounting does not create appreciable crystal stress as testified by the measured rocking curves shown in Fig.[3]

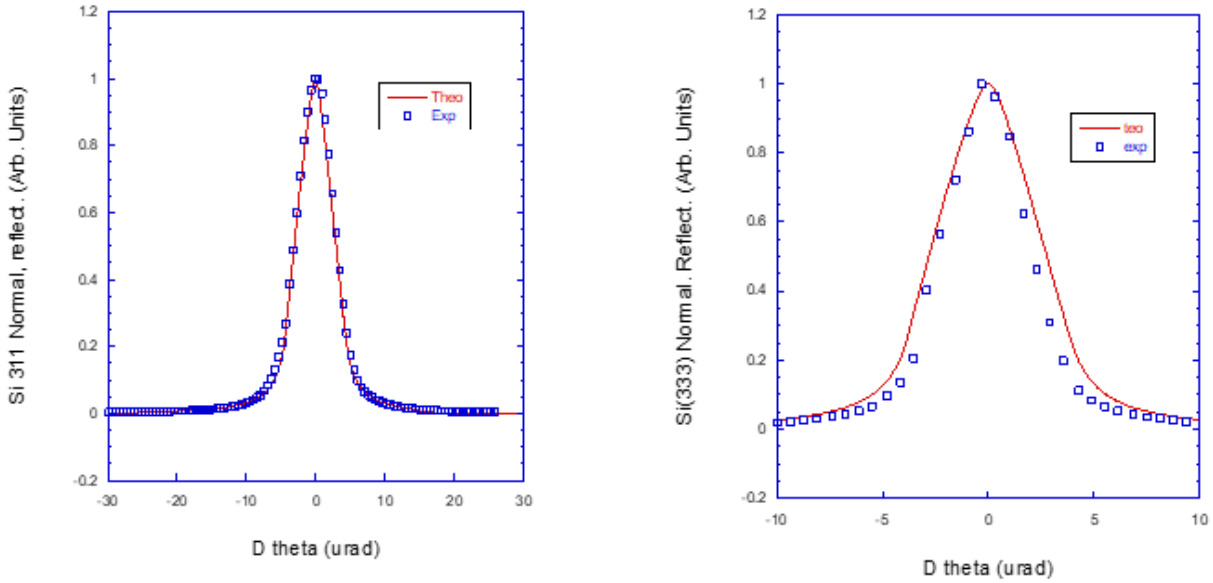

Fig.[3] Comparison of theoretical calculations (red line) and experimental data (blue symbols) on rocking curves of Si(311) crystals (left) and Si(333) crystals (right) measured respectively at 25 and 15 keV. The measured values are 6±1 µrad for Si(311) and 4±1 µrad for Si(333).

In both cases the measured rocking curves closely follow the theoretical predictions, this aspect is of paramount importance for the collection of data at high energy resolution.
A further important parameter is the photon flux available on the sample, particularly critical for the study of diluted materials. Here the flux measured with the Si(111) crystals at the maximum angular acceptance conditions of the beamline at a current of about 180 mA is shown (Fig.[4])

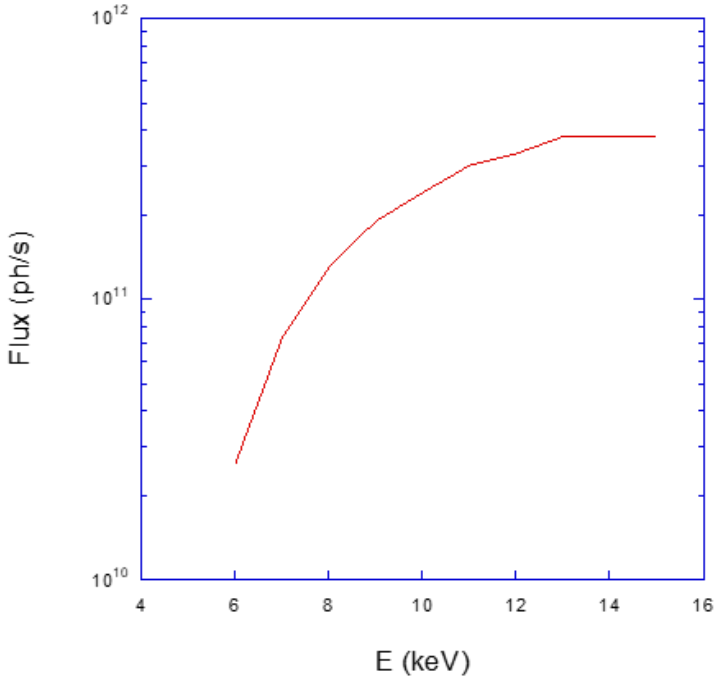

Fig.[4] Flux available at the sample position using the Si(111) crystal pair. Data collected at the maximum angular acceptance i.e. 1 mrad hor and 0.09 mrad vert, and the ring running at 180 mA.

The flux is in the order of 10^{11} ph/s the reduction at low energies being due mainly to the total thickness the Be windows (about 1mm) still present along the beamline.

The output intensity is stabilized by a continuous feedback system that can work either at a fixed absolute value or at a fixed point in the rocking curve. The energy stability of the device is shown in Fig.[5] where two consecutive spectra of a Fe foil collected with Si(311) crystals are shown with their difference:

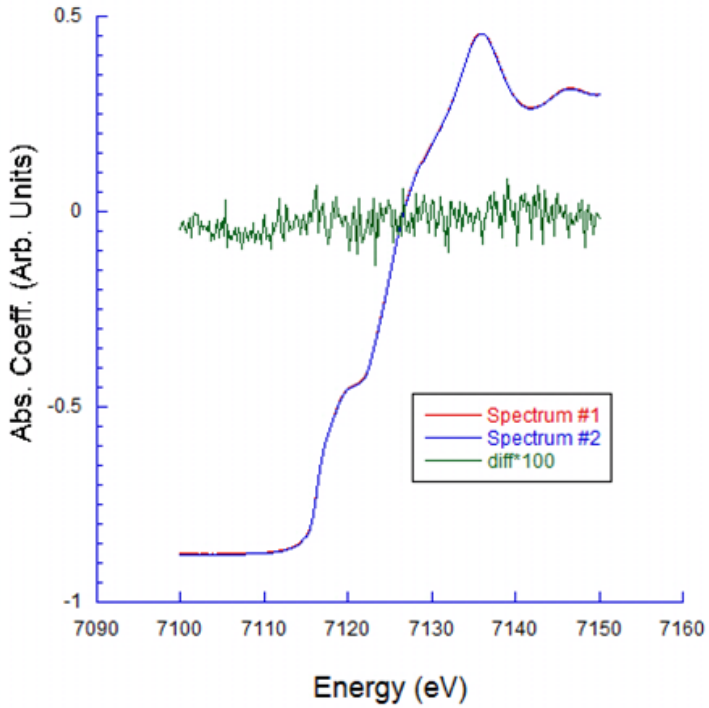

Fig.[5] Two consecutive XANES spectra of a Fe foil (blue and red) collected with Si(311) crystals. The difference of these spectra, multipled by a factor 100, is shown in green.

The difference between the two spectra contains no structure within the noise level denoting the considerable energy stability (range of meV) of the monochromator. This makes this instrument particularly well adapted to studies in differential mode like pump and probe experiments. Also noticeable is the noise level observed in transmission mode spectra that can reach values in the order of 10^{-5} units (Fig.[6]).

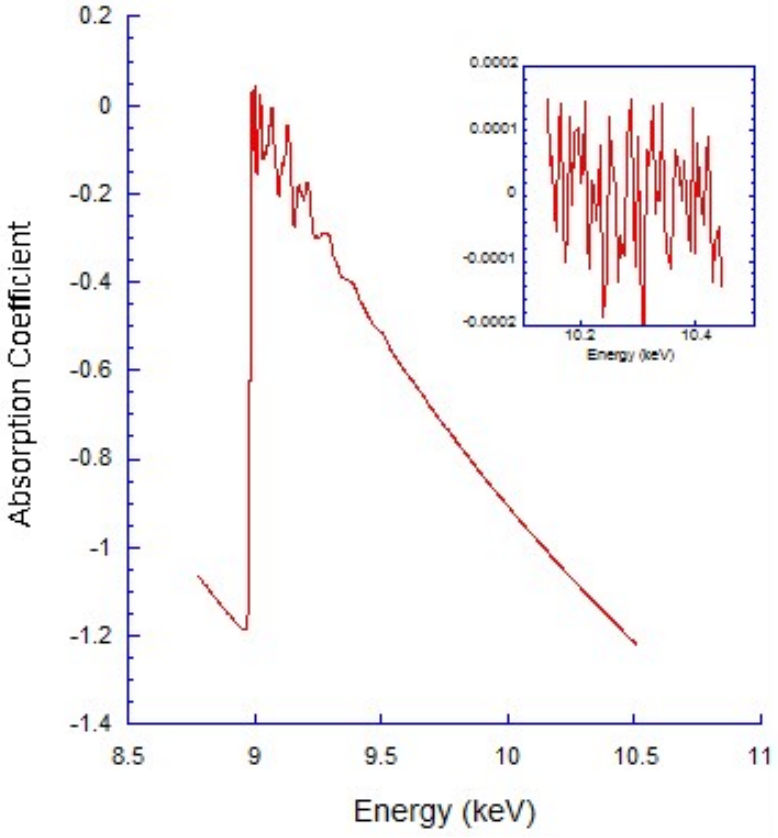

Fig.[6] . Example of spectrum of a Cu foil collected in transmission mode in EH1 with Si(111) crystals. The noise on the tail (see inset) is about $7*10^{-5}$.

Second mirror, M2

The second mirror consists in a double cylindrical channel on a single Si substrate. One of the channels is coated with Pt, the other is left with bare Si. The meridional radius of curvature can be adjusted with a motorized bender, the sagittal radius of curvature is fixed at 45.8mm. The system works in a 2:1 focusing scheme with the sample at about 18m from the mirror. Fig.[7] shows the beam shape in the focal point:

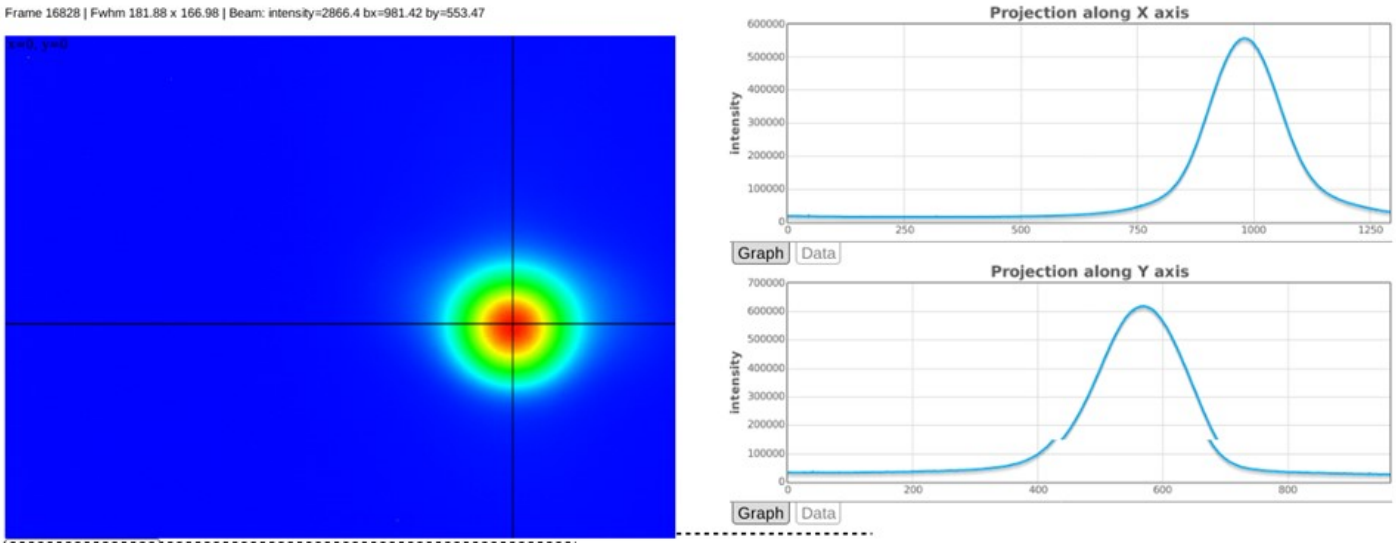

Fig.[7] Beam shape in the focal point obtained at 9 keV with Si(111) crystals and Si mirrors. The input angular acceptance was 1 mrad hor and 0.09 mrad vert. The dimensions are 180 μm hor and 160 μm vert.

This shows that the beamline can provide a beam of less than 200 *μ*m at the maximum flux. In the presented example the gain in flux on the sample within the focal spot respect to the previous GILDA project is about a factor 100.

LISA has two experimental hutches, the principal one (EH2) approximately centered on the focal position of M2 while the other (EH1) is a few meters upstream. In EH2 a long bench (Fig.[8]) with a motorized vertical movement is installed, supporting the vacuum chambers and detectors. All the elements are mounted on sliding plates along the bench in order to move them in the desired position and host even bulky instrumentation.

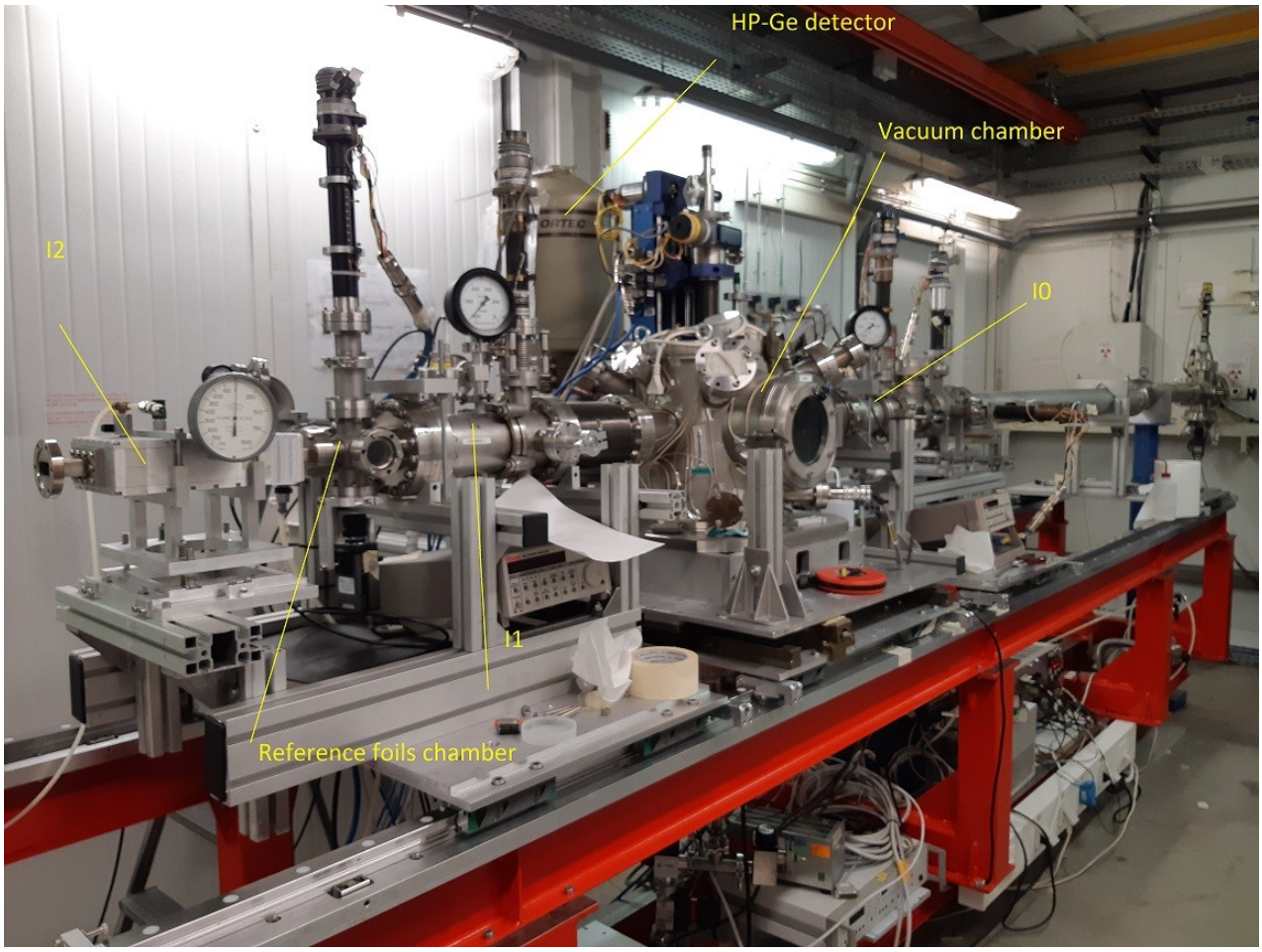

Fig.[8]. Picture of the new bench installed in EH2 with the various elements.

The main vacuum chamber is equipped with a cold finger cryostat and it is preceded and followed by the ion chambers I0 and I1. Vertical and horizontal slits upstream I0 realize the beam shaping/cleaning before the sample. Downstream I1 a small vacuum chamber hosts the reference foils and a further ion chamber (I2) registers their spectrum. The HP-Ge detector is mounted on the machine wall side of the bench and can be approached or moved away from the sample with a motorized translation. The main vacuum chamber can be removed with the help of the overhead crane to leave space for users' instrumentation. The main bench can be vertically moved for fine alignment or for changing between the configurations with/without mirrors. EH1 is equipped with a vacuum chamber and two ionization chambers. This position is ideal when carrying out measurements in transmission mode with a mm sized beam (typically 2*2 mm) as it is far from the focal point of M2 and an uniform beam can be easily obtained.

All operations for sample alignment and data collection are carried out via SPEC, and, for the more standard tasks, Graphical User Interfaces (GUIs) are available. Macros for data collection on up to 6 samples are available with GUIs for an easier operation by the user (Fig.[9]).

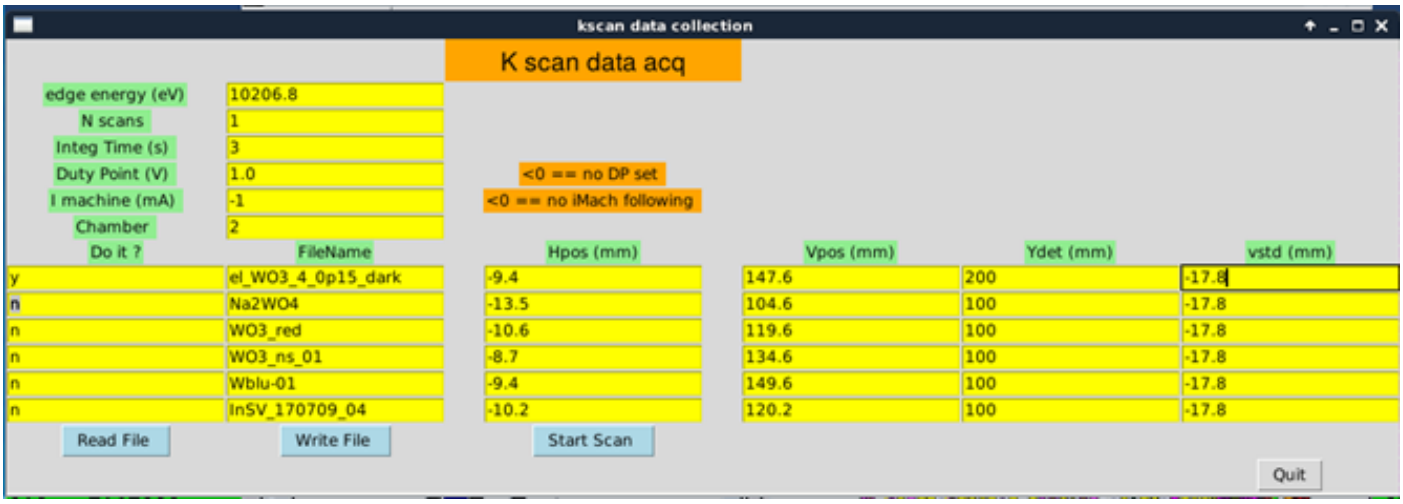

Fig.[9]. Example of a GUI for the collection of spectra on 6 samples using a constant mesh in k (photoelectron wavenumber) space. For each sample the vertical and horizontal position are defined as well as the distance of the HP-Ge detector.

Datafiles are stored in ASCII format and contain information on a large set of detector readouts, monochromator positions and machine parameters; specific routines are available for the extraction of columns of interest of the user.

Interplay between local structure and transport properties in iron-doped $LiCoPO_4$ olivines

Sergio Brutti[1,2], Jessica Manzi[1], Daniele Meggiolaro[2], Francesco M. Vitucci[2], Francesco Trequattrini[2,3], Annalisa Paolone[2], Oriele Palumbo[2]

[1]University of Basilicata, [2]CNR-ISC, [3]University of Rome

The $LiCoPO_4$ cathode (LCP) is a promising high potential positive electrode material for high energy Li-ion cells due to its very high working potential (>4.7 V vs. Li) Unfortunately, compared to the isostructural and commercially exploited $LiFePO_4$, LCP cathodes suffer poor reversibility in the first electrochemical de-insertion/insertion, a remarkable capacity fading upon cycling in lithium cells and a spontaneous self-discharge once fully charged. Some of these drawbacks can be mitigated by an appropriate tuning of the cathode composition, especially by partial substitution of the Co^{2+} with Fe^{2+}/Fe^{3+}. In this paper we illustrate in details the short and long-range structural alterations induced by iron-doping and high temperature annealing on LCP-based olivine lattice materials synthesized by a low temperature solvothermal method. Our approach exploited the synergy between X-ray diffraction (XRD) and synchrotron X-ray absorption (XAS) experiments performed at the LISA beamline in ESRF and allowed to closely relate the structural features of the lattice with the activity in lithium cells as well as with the transport properties. Four materials have been studied in order to decouple the effects of iron doping (LCP vs LCfP samples, ,) and annealing under Ar at 700°C (LCP@Ar vs. LCfP@Ar for the undoped and Fe-doped samples respectively). Focusing on the XAS experiments performed at the LISA beamline in ESRF, both the XANES and the EXAFS portions of the spectra have been acquired and analysed on two edges (iron and cobalt). The evolution of the experimental XRD patterns as well as the radial distribution functions obtained from the XAS data are shown in the figures 1 and 2.

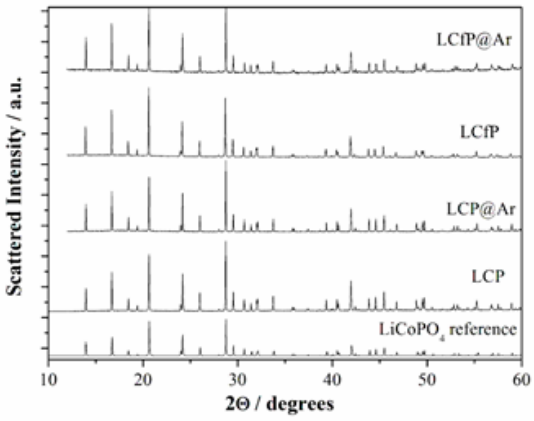

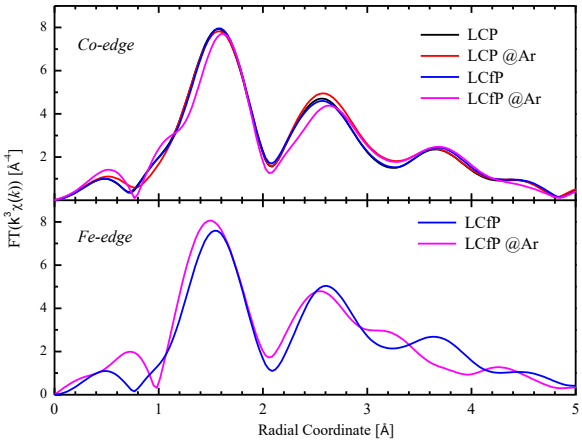

Figure 1: XRD patterns of the synthesized samples before and after the annealing at 700° C under Ar (Reproduced with permission from The Royal Society of Chemistry)

Figure 2: Radial distribution function obtained after Fourier transformation of k3χ(k) (Reproduced with permission from The Royal Society of Chemistry)

The XRD and XAS data analyses of the four LCP-based olivine materials highlight a remarkable difference in the iron oxidation state, local coordination environment around the transition metals as well as a parallel modification of the long range ordering among the studied samples. A pictorial representation of the alteration of the structure in the four samples is shown in the figure 3.

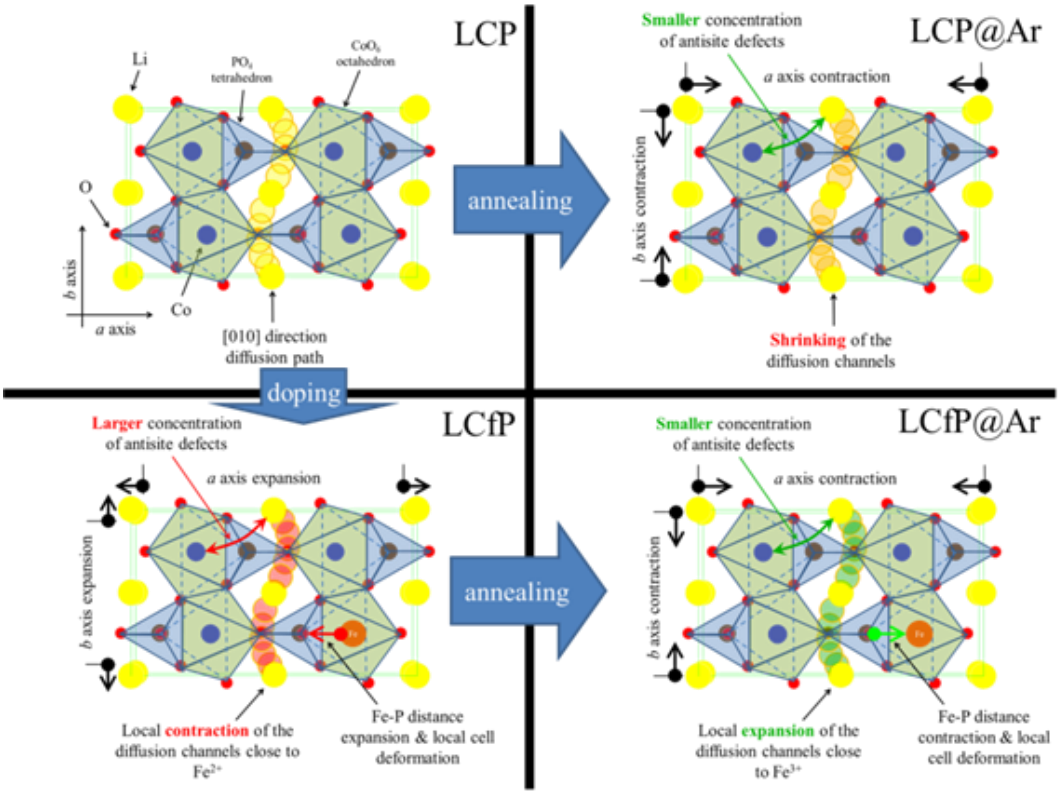

Figure 3: Pictorial representation of the alteration of the structure along the [010] lithium diffusion paths in the four samples(Reproduced with permission from The Royal Society of Chemistry)

In particular the partial substitution of cobalt ions in the olivine lattice with iron, as well as the iron oxidation state, strongly affects the long range crystal structure as well as the short range atomic coordination. These structural changes alters the concentration of anti-site defects, the natural concentration of lithium vacancies, the size of the lithium diffusion channels along the [010] direction as well as their local distortion. The balancing between these competitive effects modulates the structural breath upon electrochemical lithium de-insertion and re-insertion as well as the lithium transport properties. In particular, the incorporation of aliovalent Fe^{3+} ions due to the high temperature treatment in Ar of LCfP material leads to an enhancement of the lithium diffusion coefficient and to an increase of electrochemical lithium extraction/insertion reversibility in lithium cells.

Publication: [Journal of Materials Chemistry A 5 (2017) 14020-14030 DOI: 10.1039/c7ta03161k]

Thallium-rich rust scales in drinkable water distribution systems: a case study from northern Tuscany, Italy

Cristian Biagioni [a], Massimo D'Orazio [a], Giovanni O. Lepore [b], F. D'Acapito[b], Simone Vezzoni[a]

[a] Dipartimento di Scienze della Terra, Università di Pisa, Italy.
[b] CNR-IOM-OGG, Grenoble, France

High concentrations of thallium were found in drinkable water from the public distribution system of Valdicastello Carducci-Pietrasanta (northern Tuscany, Italy); the source of contamination was identified (the Molini di Sant'Anna spring) and isolated. However, after the replacement of the contaminant spring with a virtually Tl-free one, an increase in Tl concentration in the drinkable water was observed, suggesting the presence of a secondary source of Tl contamination.
Tl-rich scales occurring in water pipes were later identified and investigated through scanning electron microscopy, X-ray fluorescence chemical analyses, inductively coupled plasma - mass spectrometry, X-ray diffraction, and X-ray absorption spectroscopy.
Scales (with up to 5.3 wt% Tl) have been found in pipeline samples taken downstream the water treatment plant, whereas samples taken upstream contains much less Tl (~ 90 µg/g).

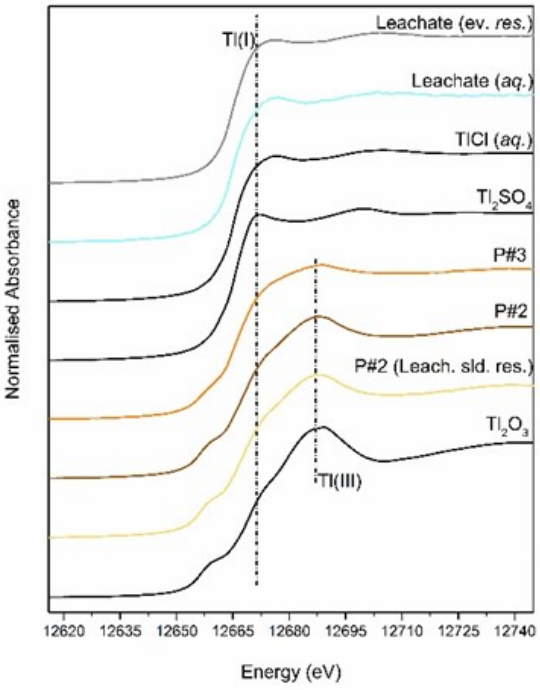

Tl L_3-edge XANES of measured samples and model compounds. Main edge crests (dashed line) are found at ~12681 and ~12687 eV for Tl(I) and Tl(III) compounds, respectively. Samples from rust scales (from P#2 to P#3 with increasing distance from the treatment plant) are congruous with those of Tl_2O_3; the presence of a shoulder in correspondence of the Tl(I) edge position suggests the presence of two different signals from both Tl(I) and Tl(III). On the other hand, the leachate samples show the presence of the sole Tl(I).

X-ray Absorption Spectroscopy (XAS) measurements on the scales were taken at **LISA-BM08** and indicated the occurrence of Tl(III), related to the presence of Tl_2O_3, as well as the occurrence of a phase containing Tl(I), likely coordinated by Cl. Indeed, the XANES region of scales downstream the treatment plant closely resemble that of Tl_2O_3 although the presence of a shoulder in correspondence of the Tl(I) edge position suggests the presence of two different signals from both Tl(I) and Tl(III).

Since leaching experiments on Tl-rich rust scales indicate that a fraction of the available Tl is easily dissolved in tap water, data were also collected on the leachate samples. Measured spectra show only the presence of Tl(I), clearly supporting the presence of a soluble Tl(I) compound. This finding promoted a further SEM investigation and finally micrometre-sized aggregates of nanometre-sized crystals of TlCl were identified. The Tl-rich nature of the scales could then be attributed to the occurrence of both nano- and micro-spherules of Tl_2O_3 and less abundant nanocrystalline µm-sized encrustations of TlCl; monovalent thallium occurring in water is therefore likely to be originated from the dissolution of TlCl encrustations.
The addition of chlorine-based oxidants in the water treatment plant partially removed Tl through oxidative precipitation of Tl_2O_3; nevertheless it also caused precipitation of soluble TlCl within the pipelines, thus originating an unexpected secondary source of contamination.

Publication: [Sci. Total Environ. 2017, 587/588, 491-501 ; doi: 10.1016/j.scitotenv.2017.02.177]

Switching Between Negative and Positive Thermal Expansion in $YFe(CN)_6$-based Prussian Blue Analogues Induced by Guest Species

Q. Gao[1], J. Chen[1], Q. Sun[2], D. Chang[2], Q. Huang[3], H. Wu[3], A. Sanson[4], R. Milazzo[4], H. Zhu[1], Q. Li[1], Z. Liu[1], J. Deng[1], X. Xing[1]

[1]Department of Physical Chemistry, University of Science and Technology Beijing, China
[2]International Laboratory for Quantum Functional Materials of Henan, Zhengzhou University, China
[3]NIST Center for Neutron Research, National Institute of Standards and Technology, Gaithersburg,USA
[4]Department of Physics and Astronomy, University of Padova, Italy

Thermal expansion of solids is critical in many technological applications and its control is a key issue for the materials design. In this regard, the occurrence of negative thermal expansion (NTE) materials offers a promising possibility to control the thermal expansion. Herein, we demonstrate that the thermal expansion of $YFe(CN)_6$-based Prussian blue analogues can be switched from giant negative to positive by introducing guest molecules (H_2O) and ions (K^+) into the void spaces of its framework structure.

$YFe(CN)_6$, without any guest ions or molecules, shows a strong NTE along all crystal axes (Fig. 1). This NTE, here observed for the first time, is larger than the isotropic NTE of the most popular ZrW_2O_8 and ScF_3. However, as soon as guest H_2O molecules are introduced into the $YFe(CN)_6$ framework, the thermal expansion is immediately switched to positive for $YFe(CN)_6{\cdot}4H_2O$, and with the further introduction of K^+ ions, an even stronger PTE is achieved in $KYFe(CN)_6{\cdot}3H_2O$ (Fig. 1). However, upon removal of H_2O molecules from $KYFe(CN)_6{\cdot}3H_2O$ to obtain $KYFe(CN)_6$, the PTE is reduced by almost a half (Fig. 1). In the absence of K^+ ions, NTE appears again in $YFe(CN)_6$. As a result, we can switch the thermal expansion of the Prussian blue analogues over a giant thermal expansion coefficient range by adjusting the concentration of guest ions or molecules.

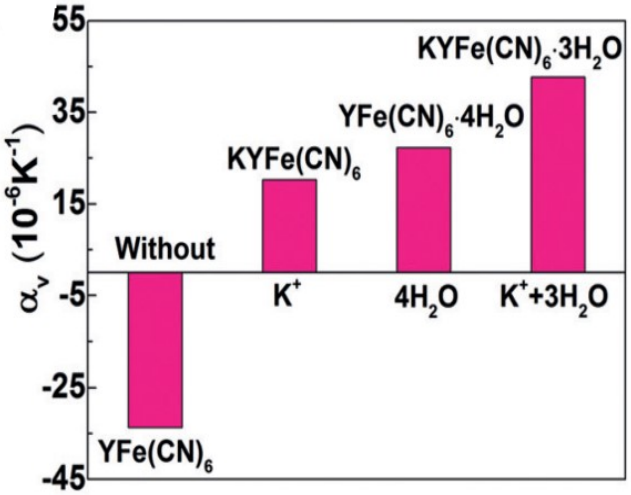

Figure 1: Volumetric thermal expansion coefficient, a_V, in $YFe(CN)_6$ and related compounds. The introduction of guest H_2O and K^+ species switches NTE to PTE behaviour.

To explain this phenomenon, we supposed that the guest ions or molecules behave as a barrier to hinder the RUM-type vibrations or, in general, transverse vibrations responsible for NTE. Accordingly, we conducted a combined EXAFS spectroscopy and neutron powder diffraction study. From NPD, we observed strong anisotropic atomic displacement parameters (ADPs) in $YFe(CN)_6$, in which the transverse ADPs of C and N atoms are much larger than the longitudinal ones (Fig. 2a,c). However, after the insertion of guest H_2O molecules, the ADPs are nearly isotropic (Fig. 2b,d) indicating that the transverse Fe-C and Y-N thermal vibrations are hindered. From the atomic mean-square relative displacements (MSRDs) determined by Fe K-edge EXAFS measurements, which take into account the correlation of the atomic motion, there are much larger transverse Fe-C vibrations in NTE $YFe(CN)_6$ than in PTE $KYFe(CN)_6$ (Fig. 2e,f).

In other words, K^+ ions have a damping effect on the transverse vibrations of C atoms, similar to H_2O molecules. These experimental results were corroborated by first-principles calculations, from which one can see that most vibrational modes with negative Grüneisen parameters in $YFe(CN)_6$ switch to positive when K^+ ions are inserted, thus resulting in PTE of $KYFe(CN)_6$.

In conclusion, the thermal expansion of the open-framework $YFe(CN)_6$-based Prussian blue analogues can be switched from negative to positive by the insertion of guest H_2O molecules or K^+ ions, whose effect is to hinder the transverse vibrations of C and N atoms responsible for NTE. This work reports a method to control the thermal expansion of NTE framework materials which may be extended to other multifunctional materials.

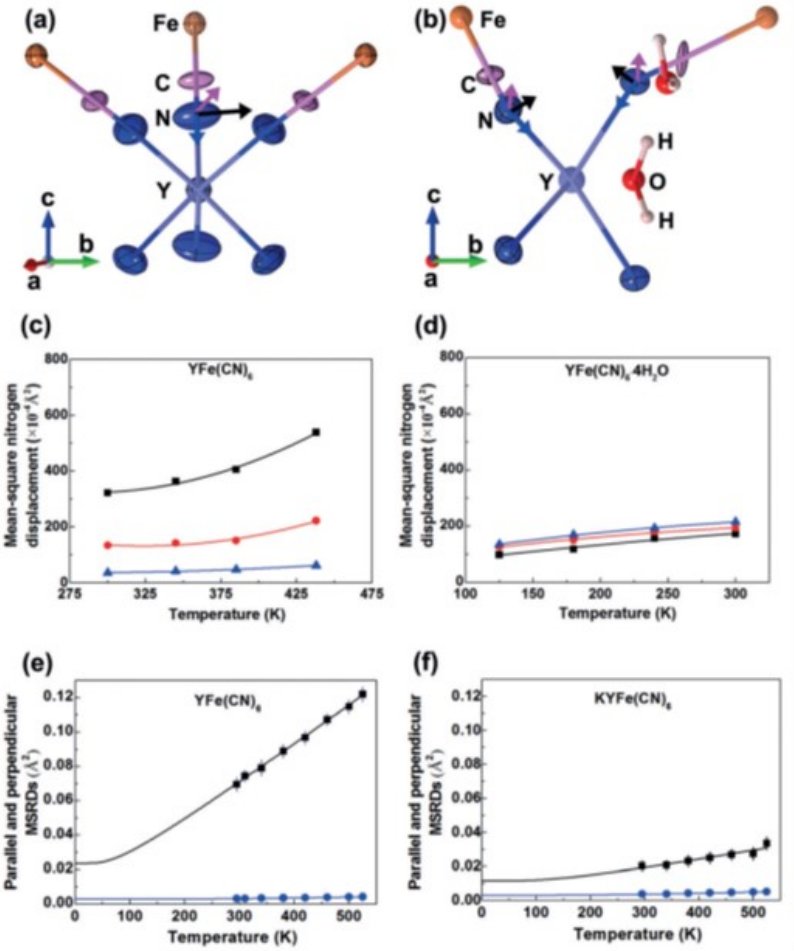

Figure 2: Thermal ellipsoids of C and N atoms in $YFe(CN)_6$ (panel a) and $YFe(CN)_6 \cdot 4H_2O$ (panel b) reconstructed from ADPs. Panels c) and d) show the corresponding transverse (■●) and longitudinal (▲) components of the mean-square displacements for N atoms as a function of temperature. Parallel (●) and perpendicular (■) MSRDs of the Fe-C atomic pair determined by EXAFS in $YFe(CN)_6$ and $KYFe(CN)_6$ are reported in panel e) and panel f), respectively. Both H_2O molecules and K^+ ions have a damping effect on the transverse vibrations of N and C atoms.

Publication: Q. Gao et al., Angew. Chem. Int. Ed. 2017, 56, 9023-9028. DOI: 10.1002/anie.201702955

Eu valence and superconductivity in $Eu_{0.5}La_{0.5}FBiSSe$ system

Y. Mizuguchi[1], E. Paris[2], T. Wakita[3], G. Jinno[1], A. Puri[4], K. Terashima[3], B. Joseph[5], O. Miura[1], T. Yokoya[3], and N. L. Saini[2]

[1]TMU Tokyo, [2]Sapienza University of Rome, [3]Okayama University, [4]ESRF Grenoble, [5]Elettra, Trieste

Superconductivity in BiS_2-based compounds, namely $REOBiS_2$ (RE = rare earth) is generally introduced by substitution in the REO layer injecting charge carriers in the BiS_2-layer hosting superconductivity. It has been found that, in addition to the charge doping, the local structure optimization is an important parameter for the physical properties of these materials [1-4]. To explore the interplay of charge and structural degrees of freedom [1,4], a new superconductor was synthesized by co-substitution in REO layer and BiS_2-layer [5]. In this compound, namely $Eu_{0.5}La_{0.5}FBiS_{2-x}Se_x$, the nominal carrier doping is 0.5 electrons per Bi site assuming that La^{3+} is substituting Eu^{2+}, with Ch (Ch = S,Se) being in the Ch^{2-} state. Figure 1 displays the superconductivity phase diagram and structure of $Eu_{0.5}La_{0.5}FBiS_{2-x}Se_x$. For small Se substitution (x = 0.0 and 0.2), filamentary superconductivity with a lower transition temperature (T_c) is observed while the bulk superconductivity appears for x>0.6 [5].

We have studied the effect of Se substitution on the Eu valence in $Eu_{0.5}La_{0.5}FBiS_{2-x}Se_x$ using X-ray absorption near edge structure (XANES) spectroscopy at LISA beamline. Eu L_3-edge XANES measurements were performed in transmission mode at room temperature. Figure 2 (left) shows normalized Eu L_3- edge XANES measured on a series of $Eu_{0.5}La_{0.5}FBiS_{2-x}Se_x$ samples. The spectra exhibit splitted white line in two peaks (peak A_1 at ~6975 eV and peak A_2 at ~6983 eV) corresponding to the transitions in the $4f^7$ and $4f^6$ final states indicating coexistence of Eu^{2+} and Eu^{3+} valence. For x = 0.0, both Eu^{2+} and Eu^{3+} peak are clearly observed, indicating the mixed valence state of Eu, as known for $EuFBiS_2$ [6]. Eu L_3- edge XANES spectrum measured sequentially on $EuFBiS_2$ is also shown with that of $Eu_{0.5}La_{0.5}FBiS_{2-x}Se_x$ for a direct comparison.

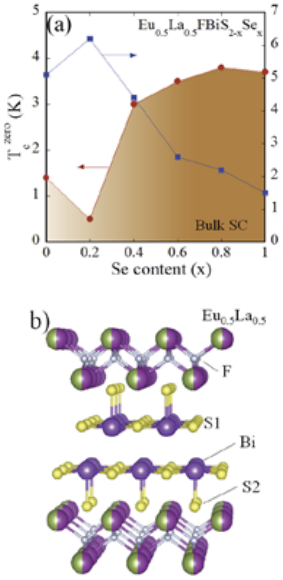

Figure 1: (a) Superconductivity phase diagram of Eu$_{0.5}$La$_{0.5}$FBiS$_{2-x}$Se$_x$. The right axis shows ρ_0 (b) Crystal structure of Eu$_{0.5}$La$_{0.5}$FBiS$_{2-x}$Se$_x$ is schematically shown for x = 0.0.

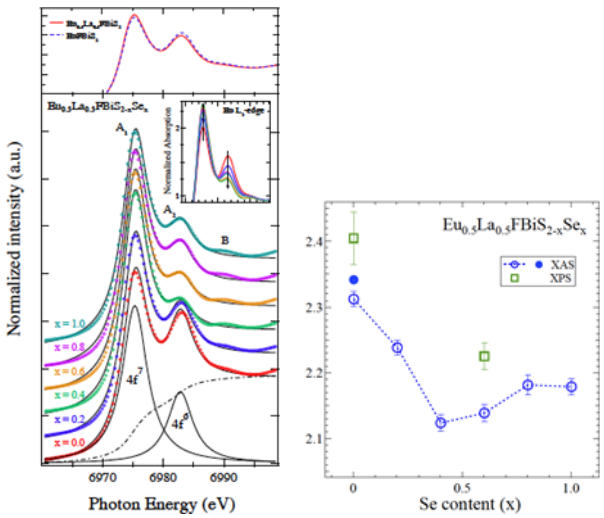

Figure 2: Eu L_3-edge normalized XANES spectra of Eu$_{0.5}$La$_{0.5}$FBiS$_{2-x}$Se$_x$. The upper panel shows Eu-L_3-edge XANES white line peaks of $EuFBiS_2$ (dashed line) compared with that of Eu$_{0.5}$La$_{0.5}$FBiS$_2$ (solid line). The right panel shows evolution of Eu valence estimated by the L_3-edge XANES.

We have estimated the average Eu valence by deconvolution of the Eu L_3-edge spectrum into Lorentzian components. The average Eu valence, calculated from the ratio of the integrated intensity of the A_1 and A_2 peaks, is ~+2.31 for x = 0.0. The Eu valence for $EuFBiS_2$ measured here is ~ +2.33 suggesting that La^{3+} substitution, that is likely to generate electrons in the conducting BiS_2 layers, hardly affects the Eu valence. This already suggests that the Eu-valence may not have a simple correlation with charge doping in the BiS_2-layer. The valence seems to be largely affected by Se substitution in the BiS_2-layer evident from the peak A_2 corresponding to $4f^6$ (Eu^{3+}) showing a suppressed intensity by Se substitution (see inset of Fig. 2). The evolution of Eu valence with Se, estimated from the XANES, is shown in Fig. 2.

With the increasing Se content, the average Eu valence decreases from ~+2.31 (for x = 0.0) to ~+2.12 (for x = 0.4) followed by a slight increase of up to ~ +2.18 for x = 0.8 and 1.0 samples. The mixed valence of Eu is also observed by core-level X-ray photoemission spectroscopy (XPS), found to be consistent with the XANES (with minor differences being due to differing probing depths). On the basis of these results we have concluded that the enhanced metallic behavior and superconductivity are not strictly related to Eu valence, but should be associated with enhanced carrier mobility caused by optimized in-plane orbital overlaps due to reduced disorder in the $BiCh_2$ layer of these materials.

References:

[1] T. Sugimoto, et al, Phys. Rev. B **89**, 201117 (2014).
[2] E. Paris, et al, J. Phys.: Condens. Matter **26**, 435701 (2014).
[3] Y. Mizuguchi, et al, Phys. Chem. Chem. Phys. **17**, 22090 (2015).
[4] Q. Liu, et al, Phys. Rev. B **93**, 174119 (2016).
[5] G. Jinno, et al, J. Phys. Soc. Jpn. 85, 124708 (2016).
[6] H. F. Zhai, et al, Phys. Rev. B **90**, 064518 (2014).

Publication: [Phys. Rev. B 95, (2017) 064515.]

Sustainable and surfactant-free high-throughput synthesis of highly dispersible zirconia nanocrystals

C. Suchomski,[*1] P. Dolcet[2,3] A. Hofmann,[1] S. Gross,[2,3] I. Djerdj,[4] B. M. Smarsly*[*1,5]

[1] *Institute of Physical Chemistry, Justus-Liebig-University Giessen, Heinrich-Buff Ring 17, 35392 Giessen, Germany.*
[2] *Istituto per l'Energetica e le Interfasi, IENI-CNR, INSTM, UdR di Padova, via Marzolo,1, 35131, Padova, Italy*
[3] *Dipartimento di Scienze Chimiche, Università degli Studi di Padova, via Marzolo, 1, 35131, Padova, Italy*
[4] *Department of Chemistry, Josip Juraj Strossmayer University of Osijek, Cara Hadrijana 8/A, 31000 Osijek, Croatia*
[5] *Center for Materials Research (LaMa), Justus Liebig University Giessen, Heinrich-Buff-Ring 16, 35392 Giessen, Germany*

Nanocrystalline ZrO_2-based ceramics gained, in recent years, more and more importance in industrial applications. The primary reasons are the enhanced mechanical, electrical, optical and catalytic properties compared to their bulk counterparts. Due to the unique combination of high fracture resistance, low thermal and high ionic conductivity, solid solutions of ZrO_2 and Y_2O_3 are widely used in oxygen sensors, hip-joint replacements, thermal barrier coatings and as electrolyte in solid oxide fuel cells.
We recently developed a microwave-assisted synthesis of ZrO_2 nanocrystals based on rational design of sol–gel reactions using tailored precursors and solvents to reduce the reaction time to the minute-scale and to achieve high yield. In order to demonstrate that the rational design of reaction pathways provides many possibilities to reduce the environmental impact of these materials, the individual synthesis steps were studied on the molecular level by means of, among others, nuclear magnetic resonance and chromatographic analysis of intermediate species.
The nanoparticles obtained through this method are almost spherical in shape with diameters ranging from 3–4 nm, and having a cubic structure, as confirmed by Rietveld refinement. Using different precursors, the particle size can be further reduced to 2–2.5 nm. The cubic structure, on the other hand, is metastable and transforms into tetragonal and monoclinic ZrO_2 after heating at 700°C, with the latter being the most stable phase. However, even minor amounts of solutes such as Y_2O_3 (e.g., 3 mol% Y) are sufficient to stabilize the tetragonal phase at 700 C, as indicated also by Raman spectroscopy. Besides, no parasitic phases such as cubic Y_2O_3 were found, regardless of the doping level.

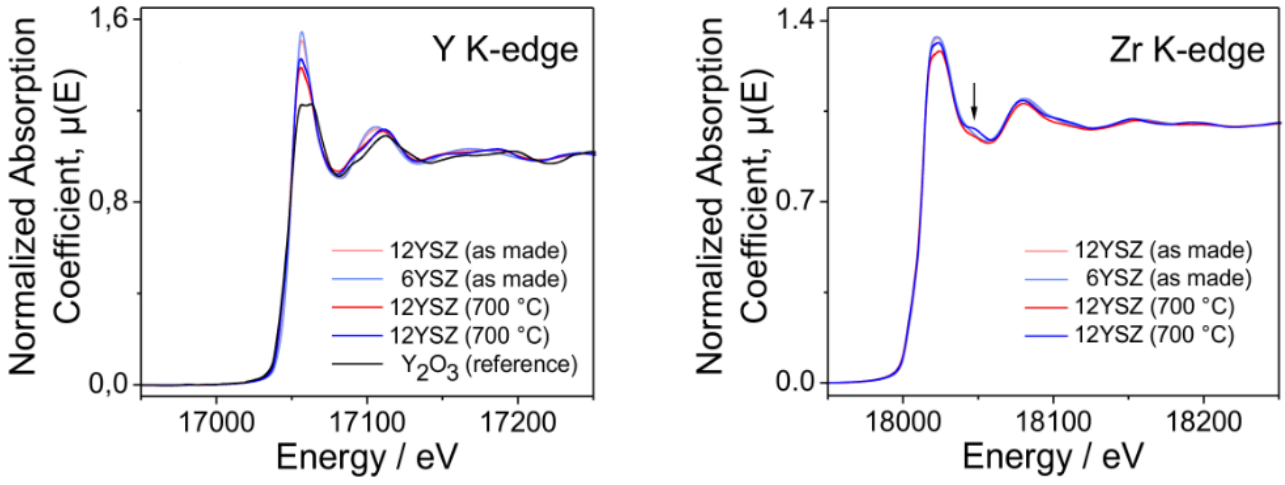

Figure 1: Y (left) and Zr (right) K-edge XANES spectra for YSZ nanoparticles with different Y content and thermal treatment

To better assess the local structural environments of Y^{3+} and Zr^{4+} in yttria-stabilized ZrO_2 (YSZ), XAS measurements were performed on samples with different Y content (6 and 12 mol% Y). In comparison to Y_2O_3 (used as reference), the Y K-edge XANES spectra of the as-made samples exhibit a significantly narrower linewidth and a much more intense white line, thus implying that the coordination number of Y^{3+} is larger than in Y_2O_3 displaying cubic bixbyite structure (i.e., > 6), and confirming the incorporation of the guest ions into the host lattice. After heat treatment at 700 °C, the XANES edges of both doped samples become broader and split into two components, suggesting a more ordered environment around yttrium.
The XANES spectra collected at the Zr K-edge are practically identical for the pristine samples without thermal treatment, which is indicative of a similar local environment around the Zr ions and comparable to cubic ZrO_2. Indeed, the fitting of the corresponding EXAFS curves determines Zr–O and Zr cation distances and coordination number being typical of cubic YSZ.
After heat treatment, the observed zirconium-related features slightly change; a bump at 18.057 keV becomes evident in the 6 mol% Y-doped sample, which can be associated with tetragonal zirconia. On the other hand, both doped materials convert into a mixed cubic-tetragonal structure upon heating, with the extent of conversion increasing with decreasing Y content.

Publication: [J. Mater. Chem. A, 2017, 5, 16296–16306]

Dependence of the Ce(III)/Ce(IV) ratio on intracellular localization in ceria nanoparticles internalized by human cells

Ferraro D.[1], Tredici I.G.[1], Ghigna P.[1], Castillio-Michel H.[2], Falqui A.[3], Di Benedetto C.[3], Alberti G.[1], Ricci V.[1], Anselmi-Tamburini U.[1], Sommi P.[1]

[1]University of Pavia, [2]ESRF, [3]King Abdullah University

CeO_2 nanoparticles (CNPs) have been recently proposed as a promising agents in the therapy of several diseases involving free radicals or oxidative stress. These nanoparticles, in fact, have been shown to be very effective as free radical scavengers with almost no toxicity, reducing the inflammation induced by ROS or RNS and preventing radiation-induced damage. For these reasons, CNPs could be a candidate for the treatment of Alzheimer's disease, as well as cerebral ischemia or hypoxia caused by stroke, promoting a neuroprotective effect on neuronal cells. However, the free radical scavenging mechanism exerted by CNPs has not yet been fully understood. The equilibrium between Ce(III) and Ce(IV) is expected to play a central role, but the presence of Ce(III) in CNPs has been questioned in abiotic mimetic experiments, while no direct prove of its presence inside the cells has ever been given. To clarify this point, we investigated *in situ* the changes in oxidation of CNPs incubated with human cells.
By *μ*-XRF maps it was possible to identify the CNP distribution within cells previously incubated for 24 h with the nanoparticles. K and Ca fluorescence lines allow to determine cell position and contours. It is apparent that Ce is present in the cells with an uneven distribution. The largest part of Ce is concentrated in few "hot spots", identified as endolysosomes, although some Ce appeared distributed, at a much lower concentration, in the rest of the cells cytoplasm.

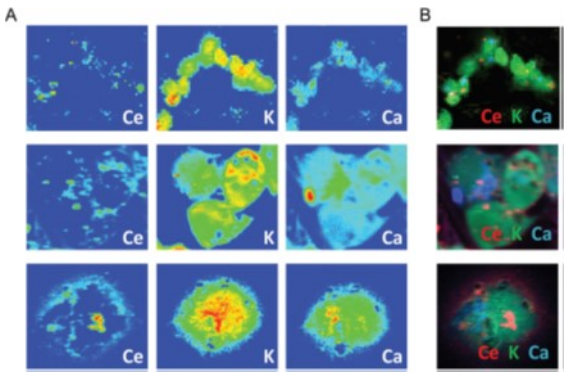

Figure 1: μ-XRF of the Ce distribution observed at three different magnifications in cells incubated with CNPs for 24 h. K and Ca distribution maps define the cell position and mark the cell contours. False-color maps show elemental concentrations within each individual image [from red (high) to blue (none)]. (B) Merged images of the elements reported in (A).

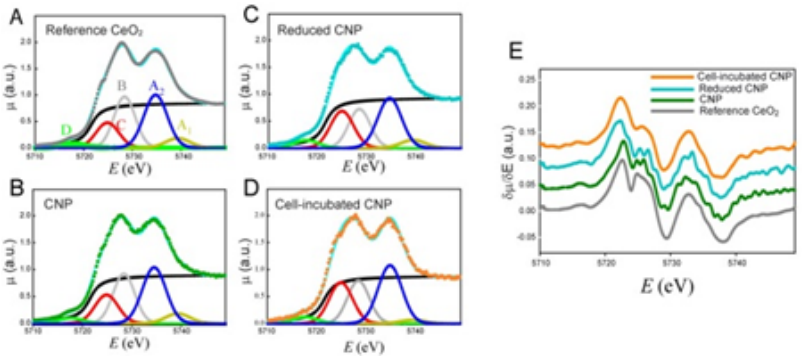

Figure 2 Ce–L_{III} XANES spectra of the reference CeO_2 (A), CNPs (B), reduced CNPs (C) and CNPs incubated with cells for 24 h (D). These panels also show the fits relative to the peak components as described in the text. Panel (E) reports the corresponding derivatives.

The oxidation state of the internalized CNPs was determined using Ce-L_{III} edge XANES, as shown in Fig. 2. To discuss better the effect of the CNP–cell interaction, the spectra relative to the CNPs incubated with the cells for 24 h (Fig. 2D) are herein compared with those of three reference materials (Fig. 2A–C). The Ce-L_{III} XANES (initial state $2p_{3/2}$) is interpreted in terms of electronic transitions to empty states; transition to continuum states with the expulsion of a photoelectron gives rise to the step with an arctan shape (black line in Fig. 2A).

All the other peaks in Fig. 2 are due to transitions to discrete empty states. In particular, the peaks labeled a_1 and a_2 are dipole-allowed transitions to empty *d* states of the electronic configuration f^0, while the b peak is a dipole-allowed transition to empty *d* states of the electronic configuration $f_1\underline{L}$, where $\underline{L}$ is a hole in the oxygen (ligand) 2*p* states. Thus, peaks a_1, a_2 and b represent different channels for electron excitation of different electronic configurations of Ce(IV): in particular, the configuration $f^1\underline{L}$ originates from the (partial) covalence of the Ce–O bond. Peak c is mixed in nature, being due to dipole-allowed transitions to *d* states of the configuration $f^1\underline{L}$, and to dipole-allowed transitions to empty *d* states of the f^1 configuration. As a result, the amplitude of peak c can be used to assess the presence of Ce(III) in the sample. Finally, peak *d* results from quadrupole-allowed/dipole forbidden excitations to the empty 4*f* states. Fig. 2B shows the spectra of the CNPs before their interaction with the biological material. The spectra are similar to those of bulk CeO_2 (Fig. 2A). A small decrease in intensity of the peaks was observed, particularly in the region of peaks c and b. This may be due to the difference in the surface to volume ratio of Ce atoms. In contrast, Fig. 2C shows the spectra relative to CNPs that were partially reduced chemically during chemical synthesis. These spectra shows an increase in the amount of Ce(III). This is better appreciated in the derivative spectra reported in Fig. 2E, clearly showing that the edge energy position of the reduced CNPs, present a shift towards a lower energy with respect to the regular CNPs and bulk CeO_2. The Ce–L_{III} XANES of CNPs incubated for 24 h with the cells is shown in Fig. 2D. The increase in the amount of Ce(III) resulting from this interaction is shown by both a marked increase in the relative intensity of peak C, and a net shift in the energy position of the edge in the derivative spectra of Fig. 2E: the spectra are then completely equivalent to those of the chemically reduced CNPs. From these analyses, it was concluded that the interaction between CNPs and cells resulted in net localization of extra electrons to Ce states, unequivocally producing Ce(III). This is the first direct evidence of the CNPs behaviour in a biological environment and, more specifically, inside cells. Overall the result shows that intracellular environments and some specific areas in the human cells can modify the oxidation state of the Ce in the CNPs. This result can be considered a significant step forward in the understanding of the biochemical mechanisms of CNPs and towards its future application in the therapy of chronic neurodegenerative disease.

Publication: [Nanoscale 9, 1527-1538(2017)]

Doping porous silicon with erbium: pores filling as a method to limit the Er-clustering effects and increasing its light emission

Guido Mula[1,2], Tony Printemps[3,4], Christophe Licitra[3,4], Elisa Sogne[5], Francesco D'Acapito[6], Narciso Gambacorti[3,4], Nicola Sestu[1], Michele Saba[1], Elisa Pinna[1,2], Daniele Chiriu[1], Pier Carlo Ricci[1], Alberto Casu[5], Francesco Quochi[1], Andrea Mura[1], Giovanni Bongiovanni[1], Andrea Falqui[5]

[1]Università degli Studi di Cagliari, Italy, [2]CNR-IOM, Italy, [3]Université Grenoble Alpes, France, [4]CEA, LETI, France, [5]KAUST, Saudi Arabia, [6]CNR-IOM-OGG c/o ESRF, LISA CRG, France

The successful emission of light from silicon structures is one of the big challenges for optoelectronics and telecommunications, that if won will allow a significant reduction of the costs and fabrication times. Unfortunately, Er clustering plays a major role in hindering sufficient optical gain in Er-doped Si materials. Even in the case of porous Si (PSi), where the large developed surface and the possibility to use an electrochemical process should allow for a better Er distribution, the long-standing failure to govern the clustering has been attributed to insufficient knowledge of the several, concomitant and complex processes occurring during the electrochemical Er-doping. Looking for an equilibrium between Er content and light emission using 1-2% Er is in any case a process from which it is difficult to expect a powerful photoluminescence, given that an insufficient Er content or the Er clustering will act as strong limiting factors. For these reasons, we propose to radically change the paradigm and use a prolonged electrochemical doping (electrochemical infiltration, EI) to obtain the filling the PSi pores with luminescent Er-rich material. To understand this process, we have to keep in mind that the electrochemical doping of a dendritic porous structure is an extremely complex task. The control of the Er infiltration mechanisms and the knowledge of what Er-rich materials are formed require a multidisciplinary approach. We resorted then to an original approach mainly based on needle electron tomography (ET), electrochemistry, EXAFS and photoluminescence (PL). Our investigations using ET clearly demonstrate that the Er deposition within the PSi pores is characterized by a heterogeneous distribution impossible to detect by the sole use of scanning electron microscopy compositional mapping. This distribution is such that Er clustering is present even for very low Er concentration, showing that just looking for an equilibrium within Er content and clustering in PSi is a blocked path. We overcame this issue by the pores filling, showing that, when the PSi pores are filled with Er-rich material, the PL emission is enhanced with respect to the simple Er doping.

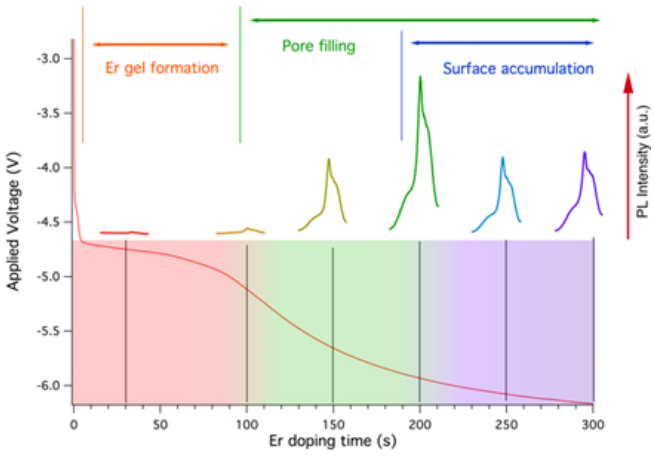

In Figure 1 we show a summary of our results, where the evolution of the electrochemical infiltration (applied voltage in a constant-current experiment) is superposed to the Er-related PL emission. In the same figure the three regions describing the three different key processes taking place during the EI process are indicated. These results demonstrate that the filled pores show an intense PL emission, significantly higher, in the given experimental configuration, that the emission from samples with standard amount of Er. For a quantitative comparison among the samples, in our experiment 200s doping time correspond to 8 at% of Er. The doping content spans linearly with EI duration.

Figure 1: Comparison of the data from the EI and PL as a function of the Er content. The black lines under the PL intensities indicate the Er doping time for that sample (the conversion from EI duration and Er content is in the text). The colored thin vertical lines are drawn to give an approximate indication of where the different EI phases described are present during an EI process.

Besides achieving an intense PL emission, the path towards optimization requires the understanding of the nature of the Er compounds within the pores formed after the thermal activation of Er. The results, showing that both Er oxide and Er silicate are present, were obtained by time-resolved PL and EXAFS.
EXAFS data at the Er-L_{III} edge were an important support to the identification of the luminescent material within the pores as a 'local' Er silicate, probably in a glassy phase. In fact, the observation of both Er-O and Er-Si neighbours resembles what is present in the crystalline silicates ($Er_2Si_2O_7$, namely) but the absence of higher coordination shells, in particular any RE-RE coordination, suggests the presence of a glassy structure in the long range. Considering that the pore developed surface is about 450 m^2/cm^3, a dominant fraction of Er ions is in the interface with the Si walls and this is the reason for the observation of the 'silicate-like' structure.

These results give a much deeper understanding of the photoluminescence origin down to nanoscale and could lead to novel approaches focused on noteworthy enhancement of Er-related photoluminescence in porous silicon.
Moreover, while unveiling the detailed effects of the electrochemical process, highlight how filling the pores with highly luminescent Er materials, could be an effective approach for improving the Er luminescence from Si materials. These results then help identifying where to address the efforts towards highly efficient Er-related emission from porous Si.

Publication: [Sci. Rep. **7** (2017), 5957.]

1. Afify N.D., Mountjoy G., Haworth R. - Selecting reliable interatomic potentials for classical molecular dynamics simulations of glasses: The case of amorphous SiO2 Computational Materials Science 128, 75-80 (2017)
2. Alberti A., Cruciani G., Martucci A. - Reconstructive phase transitions induced by temperature in gmelinite-Na zeolite American Mineralogist 102, 1727-1735 (2017)
3. Balerna A., Evangelisti C., Tiozzo C. - XAFS structural characterization of Cu vapour derived catalysts supported on poly-4-vinylpyridine and carbon X-Ray Spectrometry 46, 82-87 (2017)
4. Benedetti F., Luches P., D'Addato S., Valeri S., Nicolini V., Pedone A., Menziani M.C., Malavasi G. - Structure of active cerium sites within bioactive glasses Journal of the American Ceramic Society 100, 5086-5095 (2017)
5. Biagioni C., D'Orazio M., Lepore G.O., d'Acapito F., Vezzoni S. - Thallium-rich rust scales in drinkable water distribution systems: A case study from northern Tuscany, Italy Science of the Total Environment 587-588, 491-501 (2017)
6. Bicocchi G., Vaselli O., Ruggieri G., Bonini M., Tassi F., Buccianti A., Di Benedetto F., Montegrossi G. - Chemical alteration and mineral growth under high pCO2 conditions: Insights from the mineral chemistry of carbonate phases in the Caprese Reservoir (Northern Apennines, central Italy) Chemical Geology 450, 81-95 (2017)
7. Brutti S., Manzi J., Meggiolaro D., Vitucci F.M., Trequattrini F., Paolone A., Palumbo O. - Interplay between local structure and transport properties in iron-doped LiCoPO4 olivines Journal of Materials Chemistry A 5, 14020-14030 (2017)
8. Chinni F., Spizzo F., Montoncello F., Mattarello V., Maurizio C., Mattei G., Del Bianco L. - Magnetic hysteresis in nanocomposite films consisting of a ferromagnetic AuCo alloy and ultrafine Co particles Materials 10, 717-1-717-16 (2017)
9. Evangelisti C., Balerna A., Psaro R., Fusini G., Carpita A., Benfatto M. - Characterization of a poly-4-vinylpyridine-supported CuPd bimetallic catalyst for sonogashira coupling reactions ChemPhysChem 18, 1921-1928 (2017)
10. Ferraro D., Tredici I.G., Ghigna P., Castillio-Michel H., Falqui A., Di Benedetto C., Alberti G., Ricci V., Anselmi-Tamburini U., Sommi P. - Dependence of the Ce(III)/Ce(IV) ratio on intracellular localization in ceria nanoparticles internalized by human cells Nanoscale 9, 1527-1538 (2017)
11. Gao Q., Chen J., Sun Q., Chang D., Huang Q., Wu H., Sanson A., Milazzo R., Zhu H., Li Q., Liu Z., Deng J., Xing X. - Switching between giant positive and negative thermal expansions of a YFe(CN)6-based Prussian blue analogue induced by guest species Angewandte Chemie International Edition 56, 9023-9028 (2017)
12. Giuli G., Eisenmann T., Bresser D., Trapananti A., Asenbauer J., Mueller F., Passerini S. - Structural and electrochemical characterization of Zn1−xFexO—effect of aliovalent doping on the Li+ storage mechanism Materials 11, 49-1-49-13 (2017)
13. Minguzzi A., Naldoni A., Lugaresi O., Achilli E., d'Acapito F., Malara F., Locatelli C., Vertova A., Rondinini S., Ghigna P. - Observation of charge transfer cascades in α-Fe2O3/IrOx photoanodes by operando X-ray absorption spectroscopy Physical Chemistry - Chemical Physics 19, 5715-5720 (2017)
14. Mizuguchi Y., Paris E., Wakita T., Jinno G., Puri A., Terashima K., Joseph B., Miura O., Yokoya T., Saini N.L. - Evolution of Eu valence and superconductivity in layered Eu0.5La0.5FBiS2−xSex system Physical Review B 95, 064515-1-064515-6 (2017)

15. Montegrossi G., Giaccherini A., Berretti E., Benedetto F. Di, Innocenti M., d'Acapito F., Lavacchi A. - Computational speciation models: A tool for the interpretation of spectroelectrochemistry for catalytic layers under operative conditions Journal of the Electrochemical Society 164, E3690-E3695 (2017)

16. Mula G., Printemps T., Licitra C., Sogne E., Gambacorti N., Sestu N., Saba M., Pinna E., Chiriu D., Ricci P.C., Casu A., Quochi F., Mura A., Bongiovanni G., Falqui A. - Doping porous silicon with erbium: Pores filling as a method to limit the Er-clustering effects and increasing its light emission Scientific Reports 7, 5957-1-5957-12 (2017)

17. Niedermaier M., Dolcet P., Gheisi A.R., Tippelt G., Lottermoser W., Gross S., Bernardi J., Diwald O. - Stability and local environment of iron in vapor phase grown MgO nanocrystals Journal of Physical Chemistry C 121, 24292-24301 (2017)

18. Ottini R., Tealdi C., Tomasi C., Tredici I.G., Soffientini A., Anselmi-Tamburini U., Ghigna P. Spinolo G. - Feasibility of electron and hole injection in heavily doped strontium barium niobate (SBN50) Sr0.5Ba0.5Nb2O6 for thermoelectric applications Journal of Applied Physics 121, 085104-1-085104-8 (2017)

19. Pelli Cresi J.S., Spadaro M.C., D'Addato S., Valeri S., Amidani L., Boscherini F., Bertoni G., Deiana D., Luches P. - Contraction, cation oxidation state and size effects in cerium oxide nanoparticles Nanotechnology 28, 495702-1-495702-9 (2017)

20. Phan T.H.V., Bonnet T., Garambois S., Tisserand D., Bardelli F., Bernier-Latmani R., Charlet L. - Arsenic in shallow aquifers linked to the electrical ground conductivity: The Mekong delta source example Geosciences Research 2, 180-195 (2017)

21. Stabile P., Giuli G., Cicconi M.R., Paris E., Trapananti A., Behrens H. - The effect of oxygen fugacity and Na/(Na+K) ratio on iron speciation in pantelleritic glasses Journal of Non-Crystalline Solids 478, 65-74 (2017)

22. Suchomski C., Weber D.J., Dolcet P., Hofmann A., Voepel P., Yue J., Einert M., Möller M., Werner S., Gross S., Djerdj I., Brezesinski T., Smarsly B.M. - Sustainable and surfactant-free high-throughput synthesis of highly dispersible zirconia nanocrystalsJournal of Materials Chemistry A 5, 16296-16306 (2017)

23. Tedesco C., Brunelli M. - X-ray powder diffraction Reference Module in Chemistry, Molecular Sciences and Chemical Engineering

24. Todaro M., Sciortino L., Gelardi F.M., Buscarino G. - Determination of geometry arrangement of copper ions in HKUST-1 by XAFS during a prolonged exposure to air Journal of Physical Chemistry C 121, 24853-24860 (2017)

25. Valotto G., Cattaruzza E., Bardelli F. - Multi-edge X-ray absorption spectroscopy study of road dust samples from a traffic area of Venice using stoichiometric and environmental references Spectrochimica Acta A 173, 971-978 (2017)

26. Wolska A., Sobierajski R., Klinger D., Klepka M.T., Jacyna I., Wawro A., Jakubowski M., Kisielewski J., Kurant Z., Sveklo I., Bartnik A., Maziewski A. - Polarized XAFS study on the ultrathin Pt/Co/Pt trilayers modified with short light pulses Nuclear Instruments and Methods in Physics Research B 411, 112-115 (2017)

Contacts

Beamline responsible:	Francesco d'Acapito dacapito@esrf.fr +33 4 7688 2426 , +33 6 8936 4302
Beamline scientists:	Alessandro Puri puri@esrf.fr +33 4 7688 2859
	Giovanni Orazio Lepore lepore@esrf.fr +33 4 7688 2530
Local Contact:	+33 6 8838 6994
Beamline:	+33 4 7688 2085
Laboratory:	+33 4 7688 2743
Skype:	gilda_beamline
Administration:	Fabrizio La Manna lamanna@esrf.fr +33 4 7688 2962
Web page:	http://www.esrf.eu/UsersAndScience/Experiments/CRG/BM08/

Forthcoming proposals submission deadlines

CRG quota: May, 8th, 2017

Contributors to this issue

F. d'Acapito, A. Puri, G. O. Lepore, A. de Luisa (CNR-IOM, Grenoble), R. De Donatis (CNR-SPIN, Genova), S. Brutti (Univ. Basilicata), P. Ghigna (Univ. Pavia), A. Sanson (Univ. Padova), S. Gross (Univ. Padova), N. Saini (Univ. La Sapienza Roma), G. Mula (Univ. Cagliari)

Acknowledgements

A. Laloni, F. La Manna, A. Martin (CNR-IOM, Trieste)
E. Dettona (ESRF, Grenoble)